Cathodic ALD V_2O_5 thin films for high-rate electrochemical energy storage†

Xinyi Chen,[ab] Ekaterina Pomerantseva,[bc] Keith Gregorczyk,[ab] Reza Ghodssi[bc] and Gary Rubloff*[ab]

Atomic layer deposition (ALD) is attractive for next-generation electrical energy storage in forming passivation layers and more recently active storage material. Here we report a detailed study of ALD V_2O_5 as a high capacity cathode material, using vanadium tri-isopropoxide (VTOP) precursor with both O_3 and H_2O as oxidant. The O_3-based process produces polycrystalline films with generally higher storage capacity than the amorphous films resulting from the H_2O-based process over extended cycling (100 cycles). High capacities are achieved in V_2O_5 because of the ability to incorporate up to three Li per V_2O_5 formula unit. To address the central need for both high power and high energy, we identified the crucial tradeoff between higher gravimetric capacity with thinner films and higher material mass with thicker films. For the thickness regime 10–120 nm, we chose areal energy and power density as a useful metric for this tradeoff and found that it is optimized at 60 nm for the O_3-VTOP ALD V_2O_5 films. We believe the control of material quality, thickness, and conformality achievable with ALD processes is valuable as new nanoarchitectures for electrochemical energy storage come into sight.

Introduction

Electrochemical energy storage devices with simultaneously high power and energy densities which maintain performance during cycling have become extremely important,[1,2] particularly to efficiently manage dynamic imbalances between energy demand and the supply of energy from renewables, including solar, geothermal, wind, and wave energy. Fast energy storage (*i.e.*, high power) is also critical to the development of hybrid or all-electric vehicles, since their functionality in fast recharge, regenerative breaking, and acceleration demand high power capability while maintaining high energy to accommodate reasonable distances before recharge.

To achieve high power in electrochemical energy storage by Li-ion batteries, materials which actively store the ionic charge must be limited in thickness, because the typically slow diffusion of Li in these materials creates low power delivery for much of the stored charge. Kinetically, the diffusion time is proportional to the square of diffusion length. Thus, thin film

electrodes provide a potential solution by reducing the thickness of active storage material layers: *e.g.* reducing thickness from 1 μm to 10 nm will reduce the diffusion time by four orders of magnitude.[3,4] Efficient volumetric utilization of charge storage materials at high power accordingly requires nanoarchitectures which enable electrolyte access to large areas of thin storage films.

Atomic layer deposition (ALD) is rapidly becoming a pervasive solution for exceptional thickness and material quality control of thin films at the nanoscale. To controllably deposit ALD films in the 1–100 nm range, ALD processes use relatively low temperature growth with alternately, sequentially pulsed precursor doses, leading to self-limiting adsorption/reaction of each precursor at nominally monolayer thicknesses, with superb uniformity even over demanding topography, such as high-aspect ratio nanostructures.[5]

As a result, there has been fast growing interest in using ALD materials for energy storage because it provides key advantages over traditional thin film deposition techniques.[6–11] ALD's unprecedented capability for uniform and conformal deposition on high surface area, high-aspect ratio three-dimensional (3D) substrates, which are widely sought to enhance material loading in Li-ion battery electrodes, is expected to lead to drastic increases in areal storage density. The low temperatures (room temperature to 300 °C) characteristic of ALD processes are suitable for most current collector substrates; in contrast, chemical vapor deposition (CVD) requires higher temperatures while sol–gel methods usually need post-annealing to burn off organic materials.[12] Compared

[a]*Department of Materials Science and Engineering, University of Maryland, College Park, MD 20742, USA*

[b]*Institute for Systems Research, University of Maryland, College Park, MD 20742, USA. E-mail: rubloff@umd.edu; Fax: 301-314-9920; Tel: 301-405-3011*

[c]*MEMS Sensors and Actuators Laboratory, Department of Electrical and Computer Engineering, University of Maryland, College Park, MD 20742, USA*

† Supporting information available: Raman spectrum and TGA of ALD V_2O_5 films, EDS analysis of V_2O_5 coated Ni–TMV nanowires. See DOI: 10.1039/c3ra23031g

with physical vapor deposition (PVD) which requires high vacuum conditions, ALD can often be done in less demanding vacuum conditions, and for some processes even at atmospheric pressure.[13]

Initial application of ALD to electrical energy storage was in using ultrathin ALD layers as passivation/stabilization layers.[14,15] A few recent reports have used ALD films as active ion storage materials – mostly as anode materials for Li-ion battery structures.[7,8,10,11,16] Panda et al. demonstrated that 5 nm thick TiO_2 nanotubes produced by ALD in nanoporous alumina templates can deliver close to 100 mA h g^{-1} capacity when cycled at a high (60C) rate (nC means charge/discharge of the battery with $1/n$ hours).[10] Cheah et al. reported a self-supporting 3D electrode with 17 nm ALD TiO_2 coated on Al nanorods, which maintained 35% of the initial capacity when cycled at 20C rate.[11] ALD of TiO_2 was also demonstrated on freestanding bio-templates, showing enhanced specific capacity.[16] SnO_2 and Co_3O_4 were also deposited by ALD and demonstrated with high gravimetric capacity as anode materials in Li-ion batteries.[7,8]

In contrast, there has been very limited work reported on ALD cathode materials for Li-ion batteries so far. V_2O_5 is a well-known high capacity cathode material with a variety of deposition options available, including ALD.[17–19] There have been numerous investigations of V_2O_5 as a cathode material for Li-ion batteries, including bulk,[20] nanostructured forms,[4,21] and micron-scale thick V_2O_5 films by sputtering,[22–24] sol–gel deposition,[25] pulsed laser deposition (PLD),[26] chemical vapor deposition (CVD),[27,28] electrochemical deposition (ECD),[29] and electrostatic spray deposition (ESD).[30] However, reports on electrochemical properties of V_2O_5 by ALD are very limited.[18,19]

In this work, we systematically compare the process window, morphology, crystallinity and electrochemical performance of V_2O_5 thin films obtained from the VTOP precursor for both the new O_3-based ALD we reported recently[19] and for the traditional H_2O-based ALD. Crystalline V_2O_5 can be directly deposited using O_3 as oxidant, while amorphous films result from using H_2O as oxidant. This allows us here to evaluate the consequences of crystallinity in nanoscale V_2O_5 films with regard to electrochemical properties including gravimetric and areal capacity, energy and power density.

First, the electrochemical properties of crystalline and amorphous V_2O_5 with similar thickness (30 nm) were studied in three different voltage windows corresponding to one (4.0–2.6 V), two (4.0–2.1 V) and three (4.0–1.5 V) Li intercalation per V_2O_5 unit cell. Our results showed that crystalline films have higher capacities than amorphous ones for $1Li/V_2O_5$ (127 vs. 89 mA h g^{-1}) and $2Li/V_2O_5$ (283 vs. 219 mA h g^{-1}), while for $3Li/V_2O_5$, both films showed similar capacities stable at ~320 mA h g^{-1}. ALD films generally present higher capacity than V_2O_5 films synthesized using other thin film techniques mentioned above. Finally, using ALD's precise thickness control capability, we studied the thickness dependence of electrochemical performance of the crystalline V_2O_5 films in the range 10–120 nm. For thinner films up to 60 nm, we found areal power increased with slow decay of energy, while for 120

nm thick films a huge price of losing energy is seen when trying to push to higher power.

Experimental section

ALD processes

The ALD V_2O_5 process was developed in a commercially available BENEQ TFS 500 reactor, which has a base pressure of 2 mbar. Vanadium tri-isopropoxide [$VO(OC_3H_7)_3$, VTOP] was used as the vanadium precursor, which was kept at 45 °C giving a vapor pressure of ~0.29 torr. Ozone or water was used as the oxidant. O_3 with 18 wt% was generated from a pure O_2 source by a MKS O3MEGA ozone delivery system. The film thickness was measured ex-situ using a SOPRA GES5 spectroscopic ellipsometer. The non-uniformity is indicated by the error bars, which were standard deviations from 9 point measurements on Si wafers along the flow direction. One ALD cycle includes 0.5 s VTOP pulse, 1 s N_2 purge, 2 s oxidant pulse and 1 s N_2 purge.

Material characterizations

X-Ray diffraction (XRD) was done on a Bruker D8 Advance system with a LynxEye PSD detector and a Ni β-filter using Cu-Kα radiation (step size 0.02° in the range of $14° < 2θ < 32°$). The morphology of the ALD films was investigated by a Veeco multimode atomic force microscope (AFM) with a nanoscope III controller where Si was used as substrate. The AFM data analysis (RMS roughness and real surface area calculation) was performed using the free software Gwyddion. Transmission electron microscopy (TEM) combined with electron diffraction can provide valuable morphology, chemical and crystallinity information, however, it is difficult to prepare TEM samples for thin films unless nanoscaled substrates are used. Here, we employed Ni-coated self-assembled Tobacco mosaic virus (TMV) nanowire templates with a detailed preparation method reported elsewhere.[9,16] TEM was performed with a JEOL 2100F field emission system with energy-dispersive X-ray spectroscopy (EDS).

Li battery assembly and testing

The electrochemical properties of the V_2O_5 films were studied in standard coin cells (CR2032). All films used for electrochemical testing were grown directly on stainless steel disks. The mass of the active material was determined by weight measurements with a high precision microbalance (Mettler Toledo, XS105 dualRange, 1 μg resolution) before and after V_2O_5 deposition. Coin cells were assembled in an Ar-filled glove box with Li metal as a counter electrode and 1 M $LiPF_6$ solution in ethylene carbonate/diethyl carbonate (EC/DEC, 1 : 1 by volume) as electrolyte. An Arbin BT-2000 multichannel battery test station was used for galvanostatic life cycle and rate capability experiments. EIS data was collected from a Bio logic VMP3 using the EC-lab software.
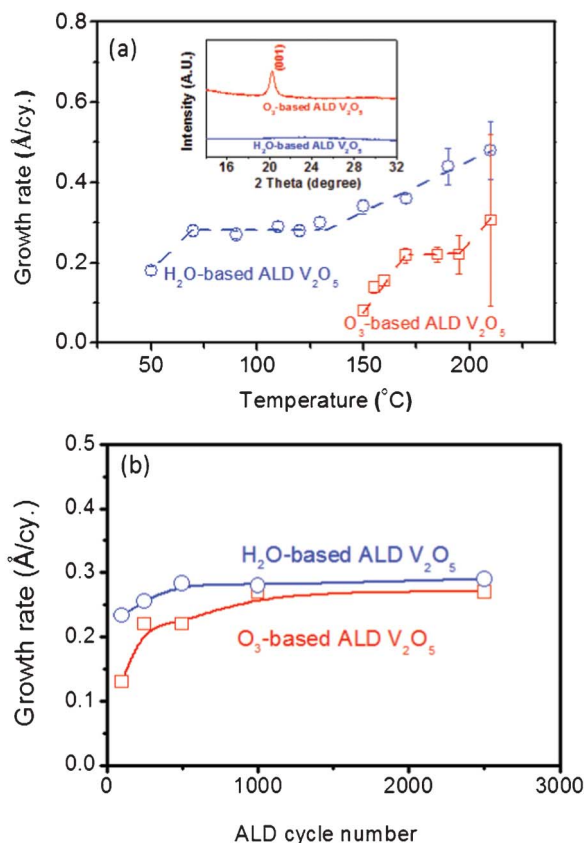
Fig. 1 (a) Temperature dependent growth rate and uniformity for O_3-based and H_2O-based ALD of V_2O_5. Error bars are indicative of non-uniformity across 4'' wafers. Dashed lines are guides to eyes. The films were grown with 500 ALD cycles. The O_3-based process shows a process window of 170–185 °C while that for H_2O-based process is 70–130 °C. The inset shows X-ray diffraction patterns for O_3-based ALD V_2O_5 prepared at 170 °C and H_2O-based ALD V_2O_5 prepared at 120 °C, indicating formation of the crystalline and amorphous films, respectively. (b) Growth rate as a function of cycle number.

Results and discussions

ALD process and film characterization

The ALD process windows for O_3-based and H_2O-based methods are indicated in Fig. 1a. As we reported previously,

the O_3 process operates in a narrow temperature window from 170–185 °C, where both stable growth rate and good uniformity were observed.[19] The H_2O-based process shows a wider temperature window with a stable growth rate between 70–130 °C. The temperature window shift is attributed to different reaction mechanisms as we have extensively discussed in a previous report.[19] Briefly, the O_3-based process is considered a combustion-like reaction while the H_2O-process is based on ligand exchange. The growth rate *vs.* cycle number was plotted in Fig. 1b, where an obvious lower growth rate was found in the first 500 cycles for O_3-based films, indicative of a significant nucleation barrier. For long ALD cycles, the growth rate of the two processes is similar at 0.28–0.3 Å/cycle.

Film crystallinity can be controlled directly by using different oxidants, as shown in the XRD patterns (inset of Fig. 1a). The O_3-based films show the characteristic (001) peak while the H_2O-based films are amorphous (full range XRD pattern of O_3-based films is available in ref. 19). To understand the temperature effect, Raman spectroscopy and thermogravimetric analysis (TGA) were conducted for the H_2O-based films deposited at 170 °C, compared to the O_3-based films deposited at the same temperature (see Fig. 1s, ESI†). For the H_2O-based films, characteristic Raman peaks were not observed and more residual water-related species were seen, indicating a significant effect of oxidant on the film crystallinity.

The two different ALD processes produced films with different surface morphology. Fig. 2 compares the morphology of the O_3-based and the H_2O-based films using AFM. The color scale was kept the same for the films with same ALD cycle number for easy comparison. The O_3-based process is featured with the formation of V_2O_5 islands, resulting in a relatively rough surface. On contrast, the H_2O-based films were very smooth. Fig. 2i summarizes the change of RMS roughness with cycle number. When ALD cycle number increased from 100 to 2500, the RMS roughness for the O_3-based films kept increasing from 0.7 to 10.4 nm while that for H_2O-based films only increased from 0.4 to 1.9 nm. Despite that, for around 70 nm thick films done with 2500 cycles, the real surface area of the O_3-based films over the projected area is 1.10, not much larger than 1.02 for the H_2O-based films.

The difference in morphology and crystallinity is also shown in the TEM images (Fig. 3), where we used Ni-coated TMV
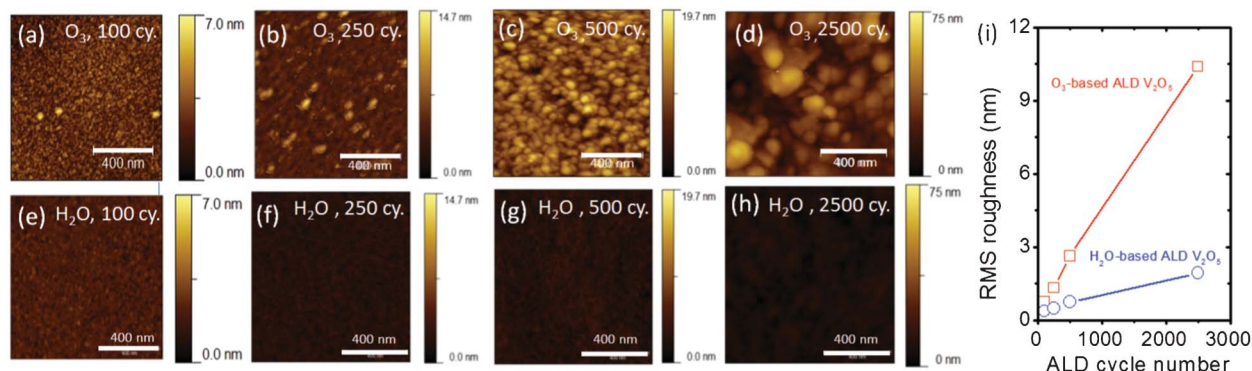
Fig. 2 AFM images of (a–d) O_3-based V_2O_5 films and (e–h) H_2O-based V_2O_5 films with different ALD cycle number, (i) RMS roughness as a function of cycle number.
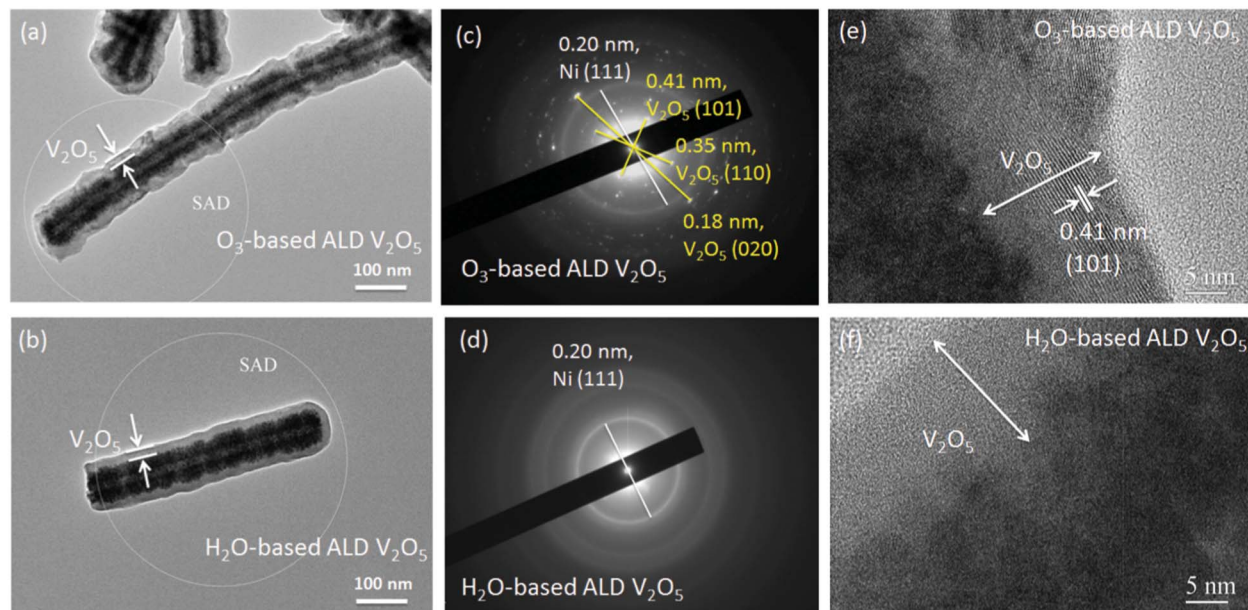
Fig. 3 (a, b) TEM images of ALD V_2O_5 films deposited on Ni-coated TMV templates with selected area diffraction (SAD) patterns shown in c and d. (e, f) HR-TEM images of ALD V_2O_5 films deposited on Ni-coated TMV templates.

nanowires as the template for V_2O_5 deposition.[9] The V_2O_5 layer was marked in the images according to detailed EDS analysis (see Fig. 2s, ESI†). In Fig. 3a and b, we observed a rougher surface of the O_3-based films, in agreement with the AFM study in Fig. 2. Moreover, the V_2O_5 thickness along the nanowire is very consistent for both processes, demonstrating the conformal coating capability on 3D substrates. The electron diffraction patterns from selected areas marked in Fig. 3a and b as ''SAD'' are shown in Fig. 3c and d, respectively. Diffraction rings from the substrate Ni were identified for both samples, while the characteristic diffraction patterns of crystalline V_2O_5 were only observed from the sample prepared by the O_3-based process, and are indexed in Fig. 3c. The characteristic V_2O_5 lattice fringe of 0.41 nm corresponding to the (101) plane is shown in high resolution TEM of O_3-based V_2O_5, while no lattice fringes can be seen for H_2O-based one (Fig. 3e and f).

The deposition of V_2O_5 films has been performed on Si for thickness measurement, Ni-coated TMV nanowires for TEM and a stainless steel disk for electrochemical characterizations. Distinguishing substrate dependencies for these cases is not easy, due to different measurement types and the mixed roles of nucleation and grain growth. However, from the TEM and XRD data, we can conclude that the three substrates studied here didn't affect crystallinity of the films, which is only relevant to the choice of oxidant – ozone or water.

Electrochemical capacity of crystalline and amorphous films

V_2O_5 films deposited on stainless steel disks were tested as cathodes in a half-cell configuration *versus* Li/Li$^+$. Three voltage ranges were chosen: 4.0–2.6, 4.0–2.1 and 4.0–1.5 V, which correspond to one, two and three lithium intercalations per V_2O_5 unit cell respectively (abbreviated below as 1Li/V_2O_5,

2Li/V_2O_5, 3Li/V_2O_5).[20] Films of roughly 30 nm thick (1000 cycles) were studied at a relatively high rate of 1C, corresponding to a current density of 147, 294 and 441 mA g^{-1} for 1Li/V_2O_5, 2Li/V_2O_5 and 3Li/V_2O_5 respectively. Because the surface area difference for the O_3-based and H_2O-based films indicated by AFM is small (less than 1.10 : 1.02), the electrochemical performance presented below should be mainly correlated with the crystallinity difference.

Fig. 4 shows discharge/charge curves for crystalline and amorphous films at the three voltage ranges selected. It is immediately noteworthy that the specific capacity of the crystalline film is greater than that for the amorphous version, independent of the state of lithiation. For 1Li/V_2O_5 (Fig. 4a), two voltage plateaus are observed for the crystalline film on both discharge and charge curves, indicating the well-defined phase transformation of α-ε-δ.[3] As expected, no plateaus were observed for amorphous films in this voltage range for a lack of phase change. The gravimetric capacity for the crystalline film is 127 mA h g^{-1} at 1C rate, consistent with our previous result.[19] Table 1 compares our results with those reported in the literature, where we have also converted their reported results into gravimetric capacity with C rate for more accurate comparison and then found the previously reported capacity of crystalline V_2O_5 in 1Li/V_2O_5 varying from 102 to 145 mA h g^{-1}, depending on the current rate and method of synthesis.[23,24,28,29] Our results for 1Li/V_2O_5 (127–142 mA h g^{-1}) are in the higher range of these values. Unfortunately the capacity of amorphous films for 1Li/V_2O_5 is not available in literature for comparison. However, it can be seen that for ALD films, crystalline films showed higher capacity than that of amorphous ones – (127 over 89 mA h g^{-1}).

Fig. 4b shows the results for 2Li/V_2O_5, presenting the additional δ-γ phase transition in crystalline V_2O_5 which
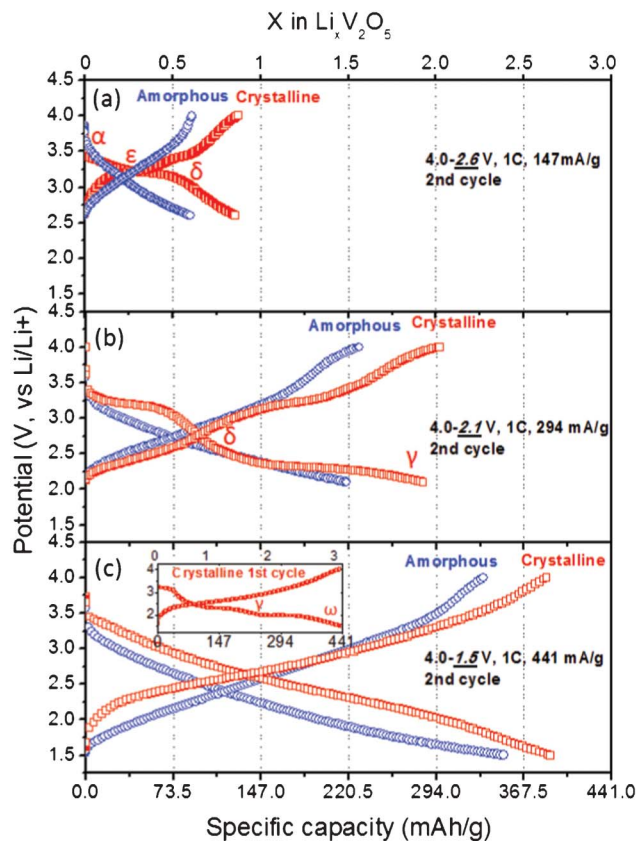
Fig. 4 Electrochemical charge/discharge curves of the cells with 30 nm thick crystalline (red square) or amorphous (blue circle) V_2O_5 films at currents for 1C rate in different voltage ranges: (a) 4.0–2.6 V for 1Li/V_2O_5; (b) 4.0–2.1 V for 2Li/V_2O_5; (c) 4.0–1.5 V for 3Li/V_2O_5.

corresponds to the plateau around 2.2 V. The gravimetric capacity for the crystalline film in 2Li/V_2O_5 range was found to be 283 mA h g^{-1}, higher than most reported values of crystalline V_2O_5 films by other techniques shown in Table 1 (204 to 300 mA h g^{-1}).[23,25–30] Again, for amorphous ALD films, no plateaus were observed in the charge/discharge curves. The capacity is 219 mA h g^{-1}, higher than 175 mA h g^{-1} for the amorphous film by electrostatic spray deposition.[30] Once again, we conclude that in the 2Li/V_2O_5 range crystalline V_2O_5 generally showed higher capacity than amorphous ones. We also note that all the reported values for crystalline V_2O_5 in this voltage range are higher than the well-known LiFePO$_4$ cathode (166 mA h g^{-1}) cycled at similar conditions (4.5–2.0 V at 2C rate), presumably due to the incorporation of the second lithium ion into the V_2O_5 unit cell.[31]

The discharge/charge curves for 3Li/V_2O_5 voltage range are shown in Fig. 4c. Another well-known phase change from γ to ω was observed around 1.8 V for the crystalline film in the first discharge curve, consistent with the phase transition observed in bulk V_2O_5.[20] The first discharge capacity of 440 mA h g^{-1} was observed, close to the theoretical value of 441 mA h g^{-1} for 3Li intercalation into the V_2O_5 unit cell. However, all the plateaus disappeared in the second charge/discharge curve due to the formation of the ω-Li$_x$V$_2$O$_5$ phase which is known to

form a solid solution.[32] The capacity dropped to 389 mA h g^{-1} in the second discharge, in agreement with literature on ω-phase cycling.[32] In this voltage range, crystalline V_2O_5 ALD films again showed advantage over those synthesized by other methods, which delivered capacity from 300 to 402 mA h g^{-1} (Table 1).[21,22,26] As expected, amorphous ALD films showed no plateaus in this voltage range, but the second discharge capacity (356 mA h g^{-1}) is close to that of crystalline films (389 mA h g^{-1}). Other reported values for amorphous films vary from 346 to 455 mA h g^{-1}, with ALD films showing the highest.[18,26] Generally, in this voltage range crystalline V_2O_5 shows comparable capacity to the amorphous one starting from the second cycle.

These specific capacities underscore two conclusions. First, the crystalline films obtained by using ozone oxidant are definitely higher than those for amorphous films from water at one and two lithium intercalation stages. Second, by comparison to previous data in Table 1, we conclude that the ALD films provide specific capacity in the upper range of the reported values. This may result, in part, from the fact that our ALD V_2O_5 films are generally thinner than those prepared by other methods, enabling more of the film to be used for energy storage at a given C rate for charging/discharging. However, as discussed above, the need for higher power at high energy requires nanostructured designs, for which thin conformal ALD layers are particularly well suited. The role of thickness is discussed in greater detail below.

Electrochemical cycling of crystalline and amorphous films

Cycling tests for crystalline and amorphous films for the three voltage ranges were performed, yielding gravimetric capacities from the 2nd to 100th cycle as summarized in Fig. 5. The ALD films are stable upon cycling, showing less than 0.15% decay per cycle when cycled for 2Li/V_2O_5 and 1Li/V_2O_5. A relatively faster decay in the first 20 cycles was observed for both crystalline and amorphous films in 3Li/V_2O_5 range, probably due to formation of a solid electrolyte interface (SEI) at low voltage. The difference of cycling degradation rates of crystalline and amorphous films for 1, 2, or 3 Li intercalation cases is not very noticeable, with amorphous films slightly more stable in the 3Li case.

We attribute at least part of the good cycling performance primarily to strong chemical bonding and good mechanical adhesion of the ALD V_2O_5 to the current collecting substrate. The relatively low temperature ALD process for depositing the V_2O_5 active storage material also reduces the risk of delamination caused by thermal stress between active material and substrate,[27] and thinner films may also reduce risk of delamination during cycling, as found in Si materials.[33] Such effects may also contribute to the generally higher capacities of ALD films compared to most other methods.

Thickness dependence

For storage applications where high power as well as high energy is important, optimizing thickness of the active storage material is a key factor. As thickness increases, total energy storage capacity increases at low rate but power, which is related to capacity at high rate, may be limited due to diffusion kinetics of ion transport in the storage material. On the other

Table 1 Electrochemical performance of V_2O_5 thin film electrodes

Crystallinity	Method[a]	Voltage (V)	Capacity (mA h g^{-1})[b]	Test rate[c]	Thickness	Ref.
For 1Li/V_2O_5						
Crystalline	ALD	4.0–2.6	142	C/3	30 nm	19
Crystalline	ALD	4.0–2.6	127	1C	30 nm	This work
Crystalline	Sputter	3.8–2.8	140	C/40	600 nm	24
Crystalline	Sputter	3.8–2.8	102	3C	2.4 μm	23
Crystalline	CVD	3.8–2.8	115	C/23	1.8 μm	28
Crystalline	ECD	3.7–2.7	145	—	—	29
Amorphous	ALD	4.0–2.6	89	1C	30 nm	This work
For 2Li/V_2O_5						
Crystalline	ALD	4.0–2.1	283	1C	30 nm	This work
Crystalline	Sol–gel	3.5–2.0	270	C/40	0.5–3 μm	25
Crystalline	PLD	4.1–2.0	250	~1C	800 nm	26
Crystalline	Sputter	3.8–2.2	204	3C	2.4 μm	23
Crystalline	CVD	3.8–2.2	220	C/23	1.5 μm	28
Crystalline	CVD	3.8–2.2	~250	~C/24	240 nm	27
Crystalline	ECD	3.7–2.0	236	—	—	29
Crystalline	ESD	4.0–2.0	~300	C/20	—	30
Amorphous	ALD	4.0–2.1	219	1C	30 nm	This work
Amorphous	ESD	4.0–2.0	175	C/20	—	30
For 3Li/V_2O_5						
Crystalline	ALD	4.0–1.5	440	1C	30 nm	This work
Crystalline	Sputter	3.7–1.5	~388	0.4–2C	230 nm	22
Crystalline	PLD	4.1–1.5	300	~1C	800 nm	26
Crystalline	ECD	3.5–1.6	402	1.3C	160 nm	21
Amorphous	ALD	4.0–1.5	356	1C	30 nm	This work
Amorphous	ALD	4.0–1.5	455	C/10	200 nm	18
Amorphous	PLD	4.1–1.5	346	~2C	310 nm	26

[a] ALD – atomic layer deposition; PLD – pulse laser deposition; CVD – chemical vapor deposition; ECD – electrochemical deposition; ESD – electrostatic spray deposition. [b] The numbers with "~" prefix are calculated from a given thickness and current density per area, assuming V_2O_5 density is 3.36 g cm^{-3}. E.g., x μAh/cm$^2 \approx \frac{3x}{y}$ mAh/g, where y is thickness in μm. [c] The numbers with "~" prefix are calculated from a given thickness and current density per area, assuming V_2O_5 density is 3.36 g cm^{-3} and a theoretic capacity of 147 mA h g^{-1} for each Li in V_2O_5. E.g., x mA/cm$^2 \approx \frac{20x}{yz}$ C, where y is thickness in μm and z is expected number of Li in V_2O_5.

hand, films too thin do not enable enough energy to be delivered at a given area. These considerations suggest, for a given materials system, an optimum thickness of storage material for achieving highest power.

To pursue this idea, we consider the thickness dependence of electrochemical properties for crystalline V_2O_5 in the 4.0–2.1 V range, where both high capacity and stable cyclability occur. We first studied gravimetric capacities of films at 1C rate with thicknesses of 10, 30, 60 and 120 nm, shown in Fig. 6. The capacities for these films are 324, 283, 230 and 198 mA h g^{-1} respectively, with the thinnest film showing highest capacity. The same trend was shown in TiO$_2$ nanotubes studied in the 2–40 nm thickness range.[10] The capacity of the 10 nm thick V_2O_5 film is higher than the theoretical value of 294 mA h g^{-1} for the 2Li/V_2O_5 range, perhaps a result of significant surface charge (double layer capacitance) to the capacity.

To explore the high power regime, we also cycled the cells with high rates up to 50C. For each C rate the cells were cycled 10 times, the rate was then increased and repeated, as shown in Fig. 7a. To compare these values, Fig. 7b plots the second cycle discharge gravimetric capacity for each C rate as normalized to that for 1C rate. In Fig. 7c the gravimetric capacity is plotted vs. film thickness. For each thickness, higher rates produce lower gravimetric capacities, and at each fixed scan rate thinner films consistently show higher

gravimetric capacities. This illustrates the tradeoff between thickness and rate performance if total power handling capability is a valued metric. We also note that at a high rate 50C, the films of 10, 30 and 60 nm can still deliver high gravimetric capacities of 164, 120 and 81 mA h g^{-1}, respectively.
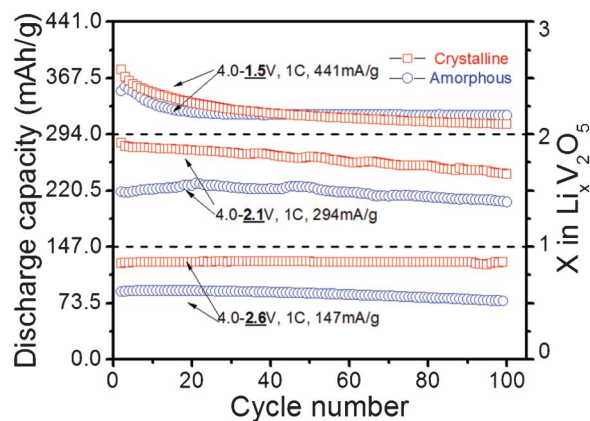
Fig. 5 Cycling performance of the cells with 30 nm thick crystalline (red square) or amorphous (blue circle) V_2O_5 films at different voltage ranges at 1C rate. Dashed lines indicate theoretic values.
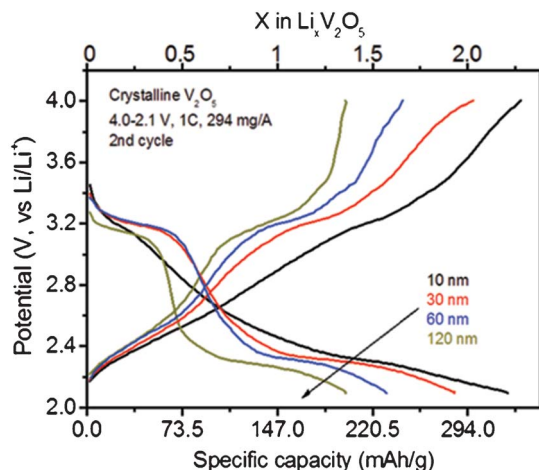
Fig. 6 Second cycle charge/discharge curves of the cells with 10–120 nm thick crystalline V_2O_5 films (4.0–2.1 V for $2Li/V_2O_5$, 1C rate).

Interestingly, we notice there is a particularly sharp capacity drop for the 120 nm thick film when the rate is increased to higher than 5C. This result is more obvious in Fig. 7b and 7c, where a large difference can be seen between the 10–60 nm films and that of 120 nm film. To understand this, we estimated the Li diffusion time τ in films as a function of thickness L. Mcgraw et al. reported the Li diffusivity D in crystalline V_2O_5 in $2Li/V_2O_5$ range as 5×10^{-14}–2×10^{-12} cm^2 s^{-1}.[34] If we take a middle value from this range, 3×10^{-13} cm^2

s^{-1}, and use the kinetic equation $\tau = L^2/2D$, we can calculate the time required for Li diffusion. The result is shown in Fig. 7d, where the corresponding C rate is also marked for reference. The diffusion time for 60 nm thick film is 60 s, corresponding to 60 C, higher than the C rates we studied here. However, for 120 nm thick films, the diffusion time is 240 s, corresponding to 15C, lower than 25C where we start to see a significant drop in gravimetric capacity. The results presented here thus suggest that Li diffusion is the limiting factor for high rate performance for the 120 nm films.

We also considered the role of electron conductivity in the V_2O_5 electrodes. The total circuit series resistant from electrochemical impedance spectroscopy (EIS) measurements (not shown here) for the cell with 120 nm V_2O_5 cathode was 20.6 Ω, which is mainly from the V_2O_5 electrode resistance and electrolyte resistance. The total voltage drop caused by this resistance is less than 0.03V, giving a current density of 14.7 A g^{-1} at 50 C for electrode mass of 91 μg. This means that the voltage difference associated with the current collector/ electrode interface and the electrode/electrolyte interface is even less than 0.03 V, i.e., too small to be responsible for the large capacity drop we observed on thick films.

A conventional Ragone plot for power and energy is shown in Fig. 8 to convey a picture of the power-energy densities of ALD crystalline V_2O_5 tested from 4.0–2.1 V for $2Li/V_2O_5$. Gravimetric features are shown in Fig. 8a, where thinner films present both higher power and energy because they have easier access to both electrons from current collector and Li$^+$ from electrolyte. To obtain a rough estimate of performance at device level, we assume a 50% mass fraction of active V_2O_5 as
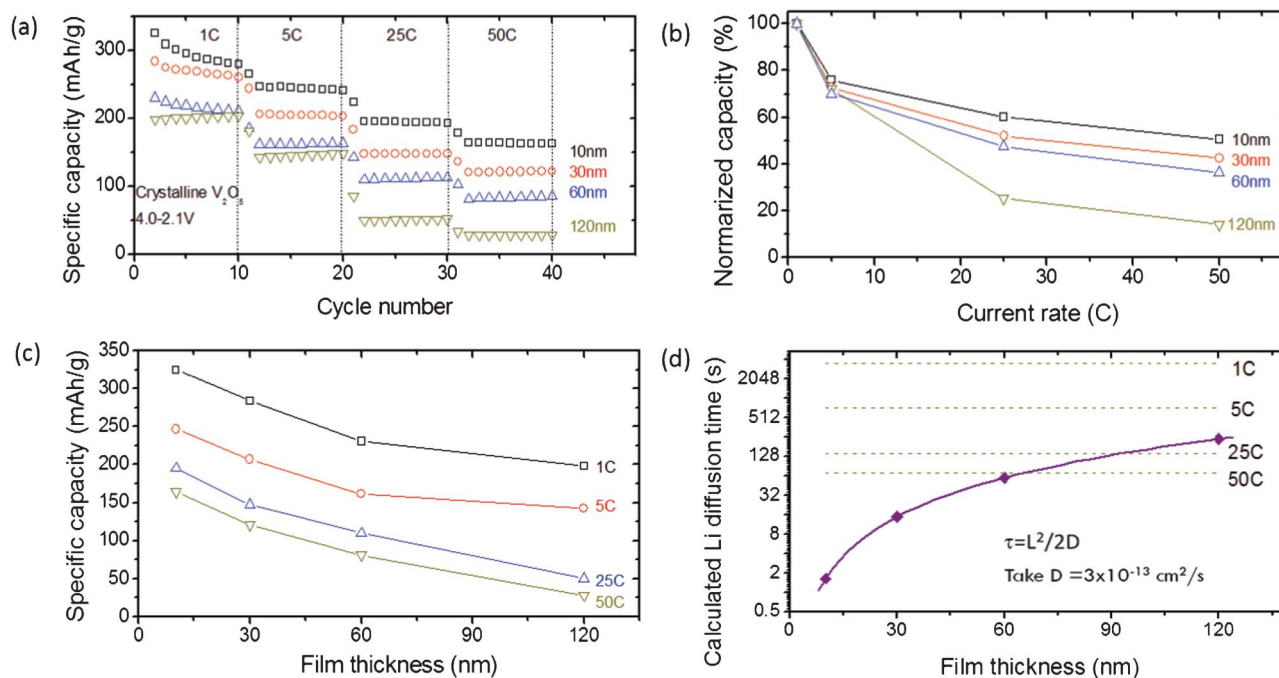
Fig. 7 (a) Rate performance of the coin cells with 10–120 nm thick crystalline V_2O_5 films in the range of 4.0–2.1 V for $2Li/V_2O_5$. The cells were cycled for 10 times at each C-rate. The data in (a) is summarized in (b) where the second cycle discharge gravimetric capacity for each C rate is normalized with that of 1C rate, and (c) where the gravimetric capacity is plotted vs. film thickness. (d) Estimated Li diffusion time for 10–120 thick V_2O_5 films, assuming a Li diffusion coefficient of 3×10^{-13} cm^2 s^{-1}.[34]
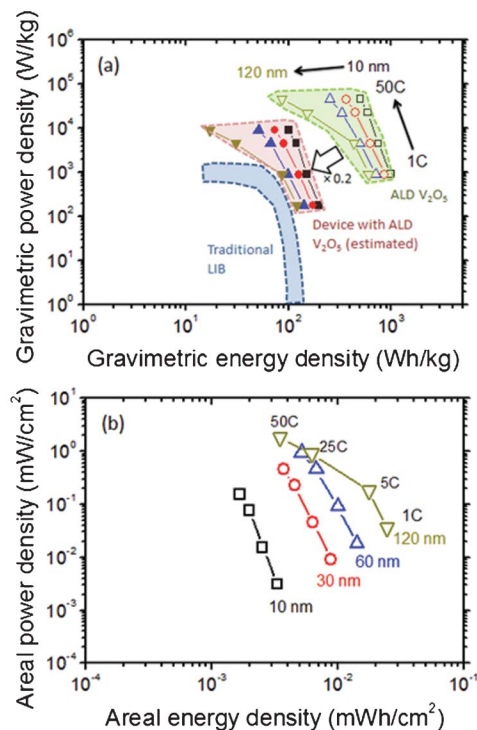
Fig. 8 (a) Gravimetric power density *vs.* energy density for the cells with 10–120 nm thick crystalline V_2O_5 films in the range of 4.0–2.1 V for 2Li/V_2O_5. The estimated device performances were plotted with a factor of 20% (50% mass fraction of V_2O_5 using MWCNT as scaffold and current collector,[35] and 40% mass fraction of cathode over device), to compare with traditional Li-ion batteries.[36] (b) Areal power density *vs.* energy density from the cells with 10–120 nm crystalline V_2O_5 films in the range of 4.0–2.1 V for 2Li/V_2O_5.

we demonstrated before using the low density and high porous multiwall carbon nanotubes (MWCNT) as scaffold and current collector.[35] Taking into account that the total cathode mass is normally around 40% of the total device, we calculated the device performance by applying a factor of 20% on the performance of V_2O_5 only, which is also shown in Fig. 8a. The estimated device performance is obviously superior to current Li-ion batteries.[36] A factor of one order increase in gravimetric power density could be expected.

If the capacities are normalized by area (Fig. 8b), we found that from 10–60 nm, both areal energy and power increase with the thickness, because increased material loading is more significant than the decrease in gravimetric capacity. In this thickness regime, the highest power of 0.93 mW cm^{-2} is achieved with total energy of 0.005 mW h cm^{-2}. Most importantly, power increase was achieved without sacrificing much energy. However, for thicker films of 120 nm, more energy can be obtained only if the cell is cycled slowly enough (1C and 5C). But for fast cycling at 25C and 50C, a higher power was achieved in the price of a significant decrease in energy. As we interpreted above, this is because of the limited Li diffusion at high rate, rendering most of the material in thick film unused. We conclude that above a certain thickness, 60 nm in this case, making thicker films will not result in better energy–power characteristic. In order to achieve high

power density per area while maintaining high energy, there should be an optimized thickness for any active material to balance the amount of material and gravimetric capacity at high current. This conclusion should apply for any substrate and therefore shine light on 3D battery designs.

Conclusions

ALD materials are attractive for electrochemical energy storage applications because thin films are required for achieving high power and the exceptional control ALD provides in material quality, thickness control, and uniformity/conformality over high surface area 3D substrates to gain more material loading. In this work, we focused on a cathode material V_2O_5 with high capacity, using VTOP precursor and comparing two oxidants, O_3 and H_2O. As proven by XRD, AFM, and TEM, the major difference is that O_3-based film is crystalline with a relatively rough surface, while H_2O-based film is amorphous and smooth. Electrochemical tests showed that ALD V_2O_5 films present higher capacity than most literature values reported using other deposition techniques. Our results on ALD films show that crystalline V_2O_5 is better than the amorphous counterpart in terms of capacity for 1Li/V_2O_5 and 2Li/V_2O_5, though their capacities are comparable for 3Li/V_2O_5. Thinner films are favored for high gravimetric capacity, especially at higher C rates. The important tradeoff between thickness and usable gravimetric capacity is clearly demonstrated for the higher-capacity crystalline material. At 120 nm thickness, capacity decreases rapidly at 25C and 50C rate, which is explained by the limited Li diffusion, while considerably thinner films suffer from limited areal capacity to support total high power. Accordingly, areal energy and power density is optimized with V_2O_5 thickness round 60 nm. We believe these kinds of investigations focusing on both power and energy will be essential for the design of next-generation 3D nanostructured electrodes for high power and energy storage devices.

Acknowledgements

References

1 J. B. Goodenough and Y. Kim, *Chem. Mater.*, 2010, **22**, 587–603.
2 J. M. Tarascon and M. Armand, *Nature*, 2001, **414**, 359–367.
3 M. S. Whittingham, *Chem. Rev.*, 2004, **104**, 4271–4301.
4 Y. Wang and G. Z. Cao, *Adv. Mater.*, 2008, **20**, 2251–2269.
5 S. M. George, *Chem. Rev.*, 2010, **110**, 111–131.
6 S. Boukhalfa, K. Evanoff and G. Yushin, *Energy Environ. Sci.*, 2012, **5**, 6872–6879.
7 M. E. Donders, H. C. M. Knoops, W. M. M. Kessels and P. H. L. Notten, *J. Power Sources*, 2012, **203**, 72–77.
8 X. F. Li, X. B. Meng, J. Liu, D. S. Geng, Y. Zhang, M. N. Banis, Y. L. Li, J. L. Yang, R. Y. Li, X. L. Sun, M. Cai and M. W. Verbrugge, *Adv. Funct. Mater.*, 2012, **22**, 1647–1654.
9 E. Pomerantseva, K. Gerasopoulos, X. Y. Chen, G. Rubloff and R. Ghodssi, *J. Power Sources*, 2012, **206**, 282–287.
10 S. K. Panda, Y. Yoon, H. S. Jung, W. S. Yoon and H. Shin, *J. Power Sources*, 2012, **204**, 162–167.
11 S. K. Cheah, E. Perre, M. Rooth, M. Fondell, A. Harsta, L. Nyholm, M. Boman, T. Gustafsson, J. Lu, P. Simon and K. Edstrom, *Nano Lett.*, 2009, **9**, 3230–3233.
12 M. D. Groner, F. H. Fabreguette, J. W. Elam and S. M. George, *Chem. Mater.*, 2004, **16**, 639–645.
13 J. S. Jur and G. N. Parsons, *ACS Appl. Mater. Interfaces*, 2011, **3**, 299–308.
14 X. B. Meng, X. Q. Yang and X. L. Sun, *Adv. Mater.*, 2012, **24**, 3589–3615.
15 Y. S. Jung, A. S. Cavanagh, A. C. Dillon, M. D. Groner, S. M. George and S. H. Lee, *J. Electrochem. Soc.*, 2010, **157**, A75–A81.
16 K. Gerasopoulos, X. L. Chen, J. Culver, C. S. Wang and R. Ghodssi, *Chem. Commun.*, 2010, **46**, 7349–7351.
17 J. Musschoot, D. Deduytsche, H. Poelman, J. Haemers, R. L. Van Meirhaeghe, S. Van den Berghe and C. Detavernier, *J. Electrochem. Soc.*, 2009, **156**, P122–P126.
18 K. Le Van, H. Groult, A. Mantoux, L. Perrigaud, F. Lantelme, R. Lindstrom, R. Badour-Hadjean, S. Zanna and D. Lincot, *J. Power Sources*, 2006, **160**, 592–601.

19 X. Y. Chen, E. Pomerantseva, P. Banerjee, K. Gregorczyk, R. Ghodssi and G. Rubloff, *Chem. Mater.*, 2012, **24**, 1255–1261.
20 M. S. Whittingham, Y. N. Song, S. Lutta, P. Y. Zavalij and N. A. Chernova, *J. Mater. Chem.*, 2005, **15**, 3362–3379.
21 Y. Y. Liu, M. Clark, Q. F. Zhang, D. M. Yu, D. W. Liu, J. Liu and G. Z. Cao, *Adv. Energy Mater.*, 2011, **1**, 194–202.
22 Y. J. Park, K. S. Ryu, K. M. Kim, N. G. Park, M. G. Kang and S. H. Chang, *Solid State Ionics*, 2002, **154**, 229–235.
23 C. Navone, S. Tintignac, J. P. Pereira-Ramos, R. Baddour-Hadjean and R. Salot, *Solid State Ionics*, 2011, **192**, 343–346.
24 C. Navone, R. Baddour-Hadjean, J. P. Pereira-Ramos and R. Salot, *Electrochim. Acta*, 2008, **53**, 3329–3336.
25 V. Vivier, J. Farcy and J. P. Pereira-Ramos, *Electrochim. Acta*, 1998, **44**, 831–839.
26 J. G. Zhang, J. M. McGraw, J. Turner and D. Ginley, *J. Electrochem. Soc.*, 1997, **144**, 1630–1634.
27 A. Mantoux, H. Groult, E. Balnois, P. Doppelt and L. Gueroudji, *J. Electrochem. Soc.*, 2004, **151**, A368–A373.
28 H. Groult, K. Le Van, A. Mantoux, L. Perrigaud and P. Doppelt, *J. Power Sources*, 2007, **174**, 312–320.
29 E. Andrukaitis, *J. Power Sources*, 2003, **119**, 205–210.
30 Y. T. Kim, S. Gopukumar, K. B. Kim and B. W. Cho, *J. Power Sources*, 2003, **117**, 110–117.
31 B. Kang and G. Ceder, *Nature*, 2009, **458**, 190–193.
32 C. Delmas, H. Cognacauradou, J. M. Cocciantelli, M. Menetrier and J. P. Doumerc, *Solid State Ionics*, 1994, **69**, 257–264.
33 M. T. McDowell, S. W. Lee, I. Ryu, H. Wu, W. D. Nix, J. W. Choi and Y. Cui, *Nano Lett.*, 2011, **11**, 4018–4025.
34 J. M. McGraw, C. S. Bahn, P. A. Parilla, J. D. Perkins, D. W. Readey and D. S. Ginley, *Electrochim. Acta*, 1999, **45**, 187–196.
35 X. Chen, H. Zhu, Y.-C. Chen, Y. Shang, A. Cao, L. Hu and G. W. Rubloff, *ACS Nano*, 2012, **6**, 7948–7955.
36 R. Mukherjee, R. Krishnan, T.-M. Lu and N. Koratkar, *Nano Energy*, 2012, **1**, 518–533.